# Design evaluation of graphene nanoribbon nanoelectromechanical devices

Kai-Tak Lam,[a] Marie Stephen Leo, Chengkuo Lee, and Gengchiau Liang[b]
*Department of Electrical and Computer Engineering, National University of Singapore, 4 Engineering Drive 3, Singapore 117576*

(Received 25 April 2011; accepted 28 May 2011; published online 19 July 2011)

Computational studies on nanoelectromechanical switches based on bilayer graphene nanoribbons (BGNRs) with different designs are presented in this work. By varying the interlayer distance via electrostatic means, the conductance of the BGNR can be changed in order to achieve ON-states and OFF-states, thereby mimicking the function of a switch. Two actuator designs based on the modified capacitive parallel plate (CPP) model and the electrostatic repulsive force (ERF) model are discussed for different applications. Although the CPP design provides a simple electrostatic approach to changing the interlayer distance of the BGNR, their switching gate bias $V_{TH}$ strongly depends on the gate area, which poses a limitation on the size of the device. In addition, there exists a risk of device failure due to static fraction between the mobile and fixed electrodes. In contrast, the ERF design can circumvent both issues with a more complex structure. Finally, optimizations of the devices are carried out in order to provide insights into the design considerations of these nanoelectromechanical switches. © *2011 American Institute of Physics*. [doi:10.1063/1.3606578]

## I. INTRODUCTION

The aggressive scaling of complementary metal oxide semiconductor devices into the sub-100 nm region has resulted in increased short channel effects and gate oxide leakage, which causes a larger power dissipation and unsatisfactory device performance.[1,2] In recent years, nanoelectromechanical systems (NEMS) have been intensively pursued as a promising solution for future low power switches in nonvolatile memory applications due to their attractive characteristics such as abrupt switching and an extremely low OFF-state leakage current ($I_{OFF}$). However, current NEMS-based switches suffer from a high activation voltage, low ON-state current ($I_{ON}$), and large static friction, also known as stiction, which can lead to device failure.[3–8] As a result, the utilization of materials with a high carrier mobility in order to obtain a large drive current at a lower bias voltage has been a major focus in NEMS research, and nanoscale materials with favorable mechanical properties and innovative designs are being studied for NEMS applications.

Carbon-based materials such as graphene, carbon nanotubes, and fullerenes have landed themselves in many NEMS applications due to their unique material properties such as high tensile strength, large thermal conductance, and high electrical carrier mobility.[9–15] Recently, bilayer graphene nanoribbon (BGNR) has become a material of interest for applications in NEMS switches. BGNR is a semiconducting material with electrical properties, such as its energy bandgap ($E_G$), that are dependent on the ribbon width, the atomic configurations at the edges, and the interlayer distance between the monolayers.[16,17] After fabrication, the conductivity of a BGNR device can be changed by varying the separation between the individual carbon layers, whereas changing the design of the NEMS component to alter the interlayer distance has a limited effect on the device's conductance. This gives us the freedom to implement different NEMS structures in order to adjust the interlayer distance using electrostatic means.

By exploiting these unique properties of BGNR, a prototype of a NEMS switching device based on the Schottky barrier field-effect transistor (SBFET), coupled with a capacitive parallel plate (CPP) floating gate design, has been shown to control the interlayer distance of the BGNR.[18] Unfortunately, this design resulted in a hysteresis loop that might not be desirable for all switching applications. Therefore, in this work, modified device structures are introduced in order to reduce the hysteresis loop in the system, and the various design parameters are evaluated for device optimization. Furthermore, we found that the BGNR NEMS switch is able to reach a high ON/OFF ratio ($I_{ON}/I_{OFF}$) that is close to 9 orders of magnitude, operating at a device bias $V_{DS}$ of 20 mV under an electrostatic doping of 0.25 eV. The relations of the switching gate bias $V_{TH}$ to design parameters such as the spring constant of the hinges and the capacitance between the electrodes are also explored in order to provide a possible design guideline. In addition, we investigate the device performance of the BGNR NEMS switch with the electrostatic repulsive force (ERF) actuator design proposed by Lee and Cho,[19] which has the potential to overcome the stiction issue at the expense of a higher design complexity.

## II. METHOD

The BGNR SBFET switching device studied was based on the model of Yan *et al.*[20] and is shown in Fig. 1, with metallic zigzag edged BGNRs (Z-BGNRs) as contacts to the channel region of the semiconducting armchair edged BGNR (A-BGNR). A similar device operating principal should hold for other metallic contacts such as aluminum

[a]Electronic mail: lamkt@nus.edu.sg.
[b]Electronic mail: elelg@nus.edu.sg.

 

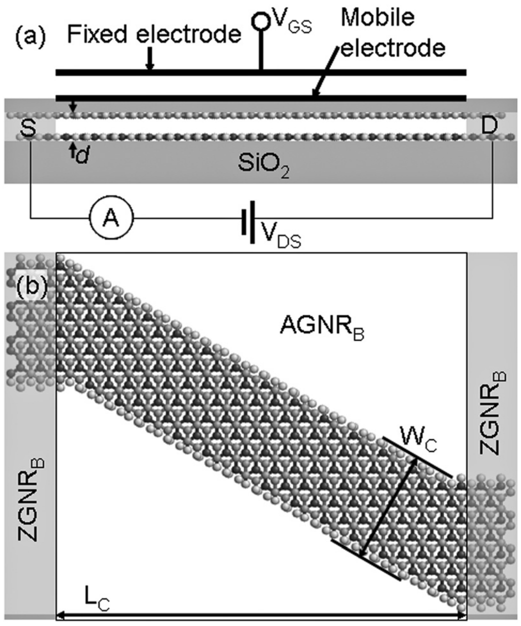


FIG. 1. (a) A device schematic of the proposed bilayer graphene nanoribbon (BGNR) nanoelectromechanical switch with a capacitive parallel plate actuator. As the gate bias $V_{GS}$ increases, the mobile electrode moves closer to the fixed electrode, increasing the interlayer distance $\boldsymbol{d}$ at the same time. (b) The top view of the BGNR switch is shown, and the ribbon width $W_C$ discussed in this work is 1.1 nm. The metallic Z-BGNR acts as the source and drain contacts.

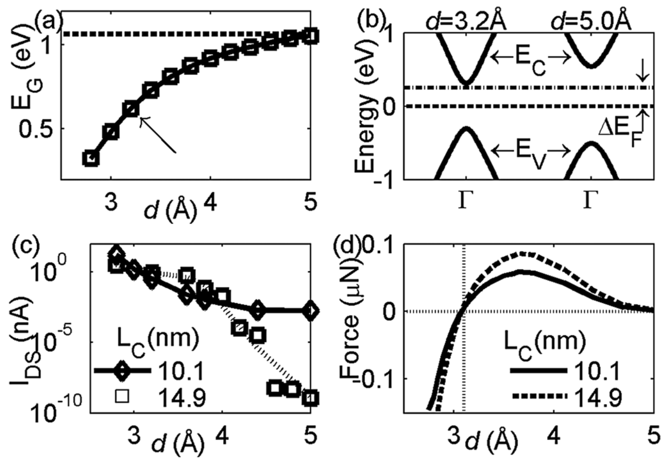


FIG. 2. (a) The energy bandgap ($E_G$) dependence on $\boldsymbol{d}$ of A-BGNR. The arrow indicates the stable distance, and as it increases, the $E_G$ also increases. The dashed line indicates the $E_G$ of the monolayer counterpart. (b) The energy band diagram showing the conduction and valance bands ($E_C$ and $E_V$) for the different interlayer distances. $\Delta E_F$ denotes the electrostatic doping. (c) The current characteristics of the switch as a function of the interlayer distance. A longer channel can improve the $I_{ON}/I_{OFF}$ ratio by decreasing the tunneling current at the OFF-state. (d) The force required to shift the interlayer distance away from its stable position. In order to increase the distance to 5 Å, about 50 nN of attractive force is needed to overcome the device geometry discussed with a channel length of 10.1 nm. The forces are approximately doubled for a channel length of 14.9 nm. A positive sign here refers to the attractive force between the layers, and a negative sign signifies repulsive forces.

and palladium, which forms a Schottky contact with A-BGNR. First, the fundamentals of the device characteristics are simulated using density-functional theory coupled with the non-equilibrium Green's function approach implemented in Atomistix Toolkit (ATK) 2008.10.[21,22] The atomic structure of the device is obtained by first relaxing a monolayer graphene nanoribbon (GNR) to a maximum planar force of 0.05 eV/Å. Next, the bilayer device is created by placing the two relaxed monolayers in the Bernel stacking order, and the interlayer distance is varied from 2.8 to 5.0 Å in order to obtain a lowest total energy at 3.1 Å. The local density approximation exchange functional is chosen to handle the many-body interactions, coupled with the double-ζ pseudopotential basis set supplied with the software. The current of the device is next calculated with $V_{DS} = 20$ mV, and the force between the monolayers at different interlayer distances is derived from the change in the total energy of the bilayer device at these distances. Analytical solutions specific to the modified CPP design are developed in order to explore the device characteristics of the NEMS switches. For the ERF actuator design, a more complex model on the force components is investigated using a finite-element method solver, COMSOL.[23]

## III. RESULTS AND DISCUSSIONS

### A. Capacitive parallel plate actuator

The operation mechanism of the BGNR NEMS switch is described in Ref. 18, and the basic principles are reiterated here for clarity. As the interlayer distance ($\boldsymbol{d}$) of a 1.11 nm wide BGNR is changed from the stable position [$\boldsymbol{d} = 3.1$ Å; see arrow in Fig. 2(a)] to 5.0 Å, the $E_G$ increases from 0.61 to 0.97 eV. By applying an electrostatic doping $\Delta E_F = 0.25$ eV, the conductance through the device is increased at $\boldsymbol{d} = 3.1$ Å due to the proximity of the Fermi-level and the conduction band as shown in Fig. 2(b). Conversely, the device conductance drops drastically as $\boldsymbol{d}$ increases due to a larger $E_G$. The currents of the devices with channel lengths ($L_C$) of 10.1 and 14.9 nm are calculated as a function of $\boldsymbol{d}$ [see Figure 2(c)]. It is observed that the $I_{ON}/I_{OFF}$ can be considerably improved by 6 orders of magnitude with the usage of the longer $L_C$ due to the reduction of the tunneling currents that dominate the $I_{OFF}$. Last, in order to verify the feasibility of the BGNR NEMS switch, the force required to change $\boldsymbol{d}$ is calculated for the ribbon areas of 11.2 and 16.5 nm$^2$, corresponding to the different $L_C$, and the result is presented in Fig. 2(d).

To reduce the hysteresis loop observed in the first design, an additional oxide layer can be placed between the fixed and mobile electrodes. By introducing an oxide capacitance ($C_{ox}$) that is less than 1/3 of the original gap capacitance ($C_{gap}$), the hysteresis loop can be eliminated completely.[24] The resultant capacitance ($C_T$) is a serial combination of both capacitances:

$$C_T = A\left(\frac{t_{gap}}{\varepsilon_{gap}} + \frac{t_{ox}}{\varepsilon_{ox}}\right)^{-1} = \frac{\varepsilon_{gap}\varepsilon_{ox}A}{\varepsilon_{ox}t_{gap} + \varepsilon_{gap}t_{ox}}, \qquad (1)$$

where $A$ is the area of the gate and is independent of the area of the active channel. The electrostatic force ($F_E$) due to the gate bias ($V_{GS}$) applied can be found via the parallel plate capacitor equation:

$$F_{\mathrm{E}} = -\frac{V_{\mathrm{GS}}^2}{2}\frac{d}{dt_{\mathrm{gap}}}C_{\mathrm{T}} = V_{\mathrm{GS}}^2\frac{\varepsilon_{\mathrm{gap}}\varepsilon_{\mathrm{ox}}^2 A}{2(\varepsilon_{\mathrm{ox}}t_{\mathrm{gap}} + \varepsilon_{\mathrm{gap}}t_{\mathrm{ox}})^2}, \quad (2)$$

where $t_{\mathrm{gap}}$ is the gap size between the fixed and mobile electrodes and changes from 5 to 0 Å. This electrostatic force is needed to balance the sum of the restorative force due to the deformed "hinges" ($F_{\mathrm{S}} = \kappa\Delta t_{\mathrm{gap}}$) and the force between the graphene layers ($F_{\mathrm{GNR}}$), i.e., $F_{\mathrm{E}} = F_{\mathrm{S}} + F_{\mathrm{GNR}}$. The relation between $V_{\mathrm{GS}}$ and $t_{\mathrm{gap}}$ is

$$V_{\mathrm{GS}} = \sqrt{\frac{2(\varepsilon_{\mathrm{gap}}t_{\mathrm{ox}} + \varepsilon_{\mathrm{ox}}t_{\mathrm{gap}})^2(\kappa\Delta t_{\mathrm{gap}} + F_{\mathrm{GNR}})}{\varepsilon_{\mathrm{gap}}\varepsilon_{\mathrm{ox}}^2 A}}. \quad (3)$$

Figures 3(a) and 3(b) show a schematic of the modified CPP and the equivalent circuit for analysis, respectively, and the current characteristics of the device, in broad lines, are presented in Figs. 3(c) and 3(d) for $L_{\mathrm{C}} = 10.1$ and 14.9 nm, respectively. The characteristics of the reference design in Ref. 18, in thin lines, are included for comparison. It can be seen in Fig. 3(c) that the hysteresis loop can be eliminated using the modified CPP actuator at the expense of increasing the $V_{\mathrm{TH}}$ from 9.75 to 22.0 V [arrows in Fig. 3(c)] due to the increase in the total capacitance with the additional $C_{ox}$. However, with a longer channel length [see Figure 3(d)], a small hysteresis loop can still be observed, and the $V_{\mathrm{TH}}$ is increased from 8.81 to 19.2 V. The reason for the small hysteresis loop in the longer channel length case is the presence of the $F_{\mathrm{GNR}}$, which have a non-linear behavior with respect to the change in $d$ as shown in Fig. 2(d). When the ratio between $F_{\mathrm{E}}$ and the sum of $F_{\mathrm{S}}$ and $F_{\mathrm{GNR}}$, i.e., $p = F_{\mathrm{E}}$ / $(F_{\mathrm{S}} + F_{\mathrm{GNR}})$, is plotted with respect to the change in $t_{\mathrm{gap}}$, shown in Fig. 4(a), the linearity brought about by the modified CPP design is disrupted by the presence of $F_{\mathrm{GNR}}$ [blue

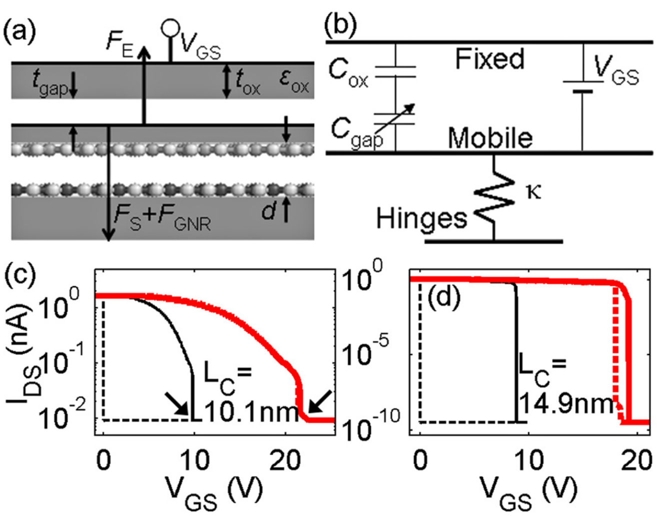


FIG. 3. (Color online) (a) An additional layer of oxide is placed between the fixed and mobile electrodes in order to modulate the device's behavior. (b) The total capacitance across the electrodes. The current characteristics of the floating gate design with (thick lines) and without (thin lines) the added oxide layer for channel lengths ($L_{\mathrm{C}}$) of (c) 10.1 and (d) 14.9 nm. The solid and dashed lines indicate increasing and decreasing $V_{\mathrm{GS}}$, respectively, and the region enclosed by them is the hysteresis loop. The spring constant $\boldsymbol{\kappa} = 1$ N/mm for all cases.

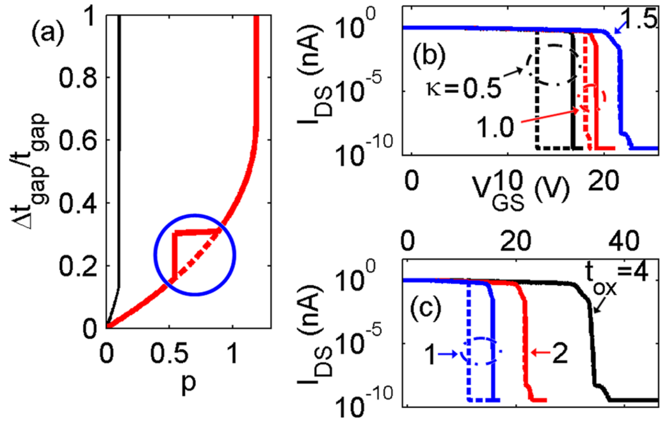


FIG. 4. (Color online) (a) The relationship between the change in gap thickness ($\Delta t_{\mathrm{gap}}/t_{\mathrm{gap}}$) and the ratio $\boldsymbol{p} = F_{\mathrm{E}}/(F_{\mathrm{S}} + F_{\mathrm{GNR}})$ for the original (thin line) and modified (thick line) CPP designs. The thick dashed line represents the case of $F_{\mathrm{GNR}} = 0$, which indicates that the $F_{\mathrm{GNR}}$ disrupts the linearity of the device, resulting in the hysteresis loop. The device characteristics are shown for (b) different spring constants $\boldsymbol{\kappa}$ (in N/mm) and (c) different oxide thicknesses $t_{\mathrm{ox}}$ (in nm). The oxide dielectric constant is set at 4.

solid circle in Fig. 4(a)]. The effect of $F_{\mathrm{GNR}}$ can be reduced by increasing $F_{\mathrm{S}}$, i.e., increasing the spring constant, which can be achieved by modifying the design of the "hinges."

The current characteristics of a long channel device with different spring constants are investigated as shown in Fig. 4(b). It is observed that a higher spring constant eliminates the hysteresis loop whereas a smaller spring constant increases it, as expected from the explanation above. In addition, the hysteresis characteristic is also affected by $C_{\mathrm{ox}}$, with a smaller $C_{\mathrm{ox}}$ (larger $t_{\mathrm{ox}}$) reducing the hysteresis loop and a larger $C_{\mathrm{ox}}$ (smaller $t_{\mathrm{ox}}$) increasing it, as shown in Fig. 4(c). This is due to the change in the linear region shown in Fig. 4(a) as the $C_{\mathrm{ox}}$ varies. It is further observed that the $V_{\mathrm{TH}}$ is also affected by both the spring constant and the $C_{\mathrm{ox}}$, i.e., we see increasing $V_{\mathrm{TH}}$ with increasing spring constant and decreasing $C_{\mathrm{ox}}$. The resulting optimization plots for $V_{\mathrm{TH}}$ and the size of the hysteresis loop (dV) with respect to the sprint constant and the $C_{\mathrm{ox}}$ are presented in Fig. 5 for the long channel device. Appropriate values for these two parameters can be chosen for different $V_{\mathrm{TH}}$ and dV requirements.

### B. Electrostatic repulsive force actuator

Having investigated the device characteristics of a BGNR NEMS switch using a modified CPP actuator, we now focus on the electrostatic repulsive force actuator design proposed by Lee and Cho.[19] A three dimensional schematic is shown in Fig. 6(a), with the accompanying top, side, and cross section views given in Figs. 6(b)–6(d), respectively. In principle, the ERF actuator design consists of four electrodes as shown in Figs. 6(b) and 6(c): two fixed peripheral electrodes at the sides, and two aligned electrodes (a top mobile electrode and a bottom fixed electrode). The two aligned electrodes form a parallel plate capacitor structure with a sandwich of layers in the following order: electrode–oxide–GNR–air gap–GNR–oxide–electrode [see Figure 6(d)]. The air gap distance is equal to the interlayer distance $\boldsymbol{d}$ between the two GNR layers, and it is at 3.1 Å initially. The

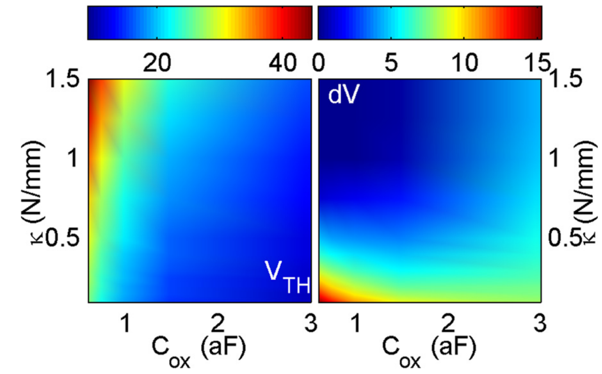


FIG. 5. (Color online) The optimization plot for $V_{TH}$ and the hysteresis loop (dV) with respect to the spring constant **κ** and the oxide capacitance $C_{ox}$. The unit of the gradation bars representing the respective plots is V.

dimensions of the top and bottom aligned electrodes are $15(L) \times 5(W) \times 1(T)$, where $L$, $W$, and $T$ represent the length, width, and thickness in nm, respectively. The dimensions of the peripheral electrodes are $15 \times 5 \times 10$ nm$^3$, i.e., 10 times thicker than the aligned electrodes Although the materials considered in this study are poly-silicon for the electrodes and silicon dioxide for the oxide layers, in principle, the electrodes can be of any metal, and any insulating material can be used as the oxide.

The device operation and the principle of the ERF actuator are described briefly as follows. A potential of $+V_E$ and $-V_E$ is applied to the peripheral electrodes and to the aligned electrodes, respectively. As a result of this potential difference, an asymmetrical electric field is set up as shown in Fig. 7, which is obtained from the finite-element solver in COMSOL. It is observed that the electric field at the top surface of the mobile electrode is greater than that at the bottom surface, and the field lines are also much denser at the top surface. This imbalance in the electric field strength results in a large upward force that pulls the aligned electrodes apart and increases the interlayer distance between the GNRs. The upward force is termed "repulsive" with respect to the aligned electrodes, but in fact it is an attractive force between the mobile electrode and the peripheral electrodes (unlike in the CPP actuators, there is no contact between any electrodes). This is a major advantage to NEMS switch applications, as the issue of stiction is eliminated.[25,26] The change in the interlayer distance is dependent on the magnitude of $V_E$, and the repulsive electrostatic force $F_E$ experienced by the top mobile electrode is

$$F_E = V_E^2 L \frac{\partial C}{\partial d}, \tag{4}$$

where $C$ represents the capacitance between the top mobile electrode and the peripheral electrodes, and $L = 15$ nm is the length of the electrode. Once the top electrode starts to move up, a restorative force $F_S$ is developed in the hinges, similar to the modified CPP case described above. Also similar to the modified CPP case above, the $F_E$ has to balance out the summation of $F_S$ and $F_{GNR}$ as shown in Fig. 6(e).

The current characteristics of this design are obtained by coupling the multi-physics software COMSOL model with the current data as a function of the interlayer distance from ATK as in the previous cases. First, the electric field configuration was calculated as shown in Fig. 7. The force on the top electrode for different $V_E$ was calculated by performing a parametric analysis on the 3D model of the device. By balancing the force equation relating $F_{GNR}$, $F_S$, and $F_E$, we obtain the device response of the ERF actuated NEMS switch, as shown in Fig. 8, with $L_C = 14.9$ nm, $t_{ox} = 1$ nm, and $V_{DS} = 20$ mV. An abrupt change from the ON-state to the OFF-state is observed, and the $V_{TH}$ is 19 V, comparable to that of the CPP design, without any hysteresis loop.

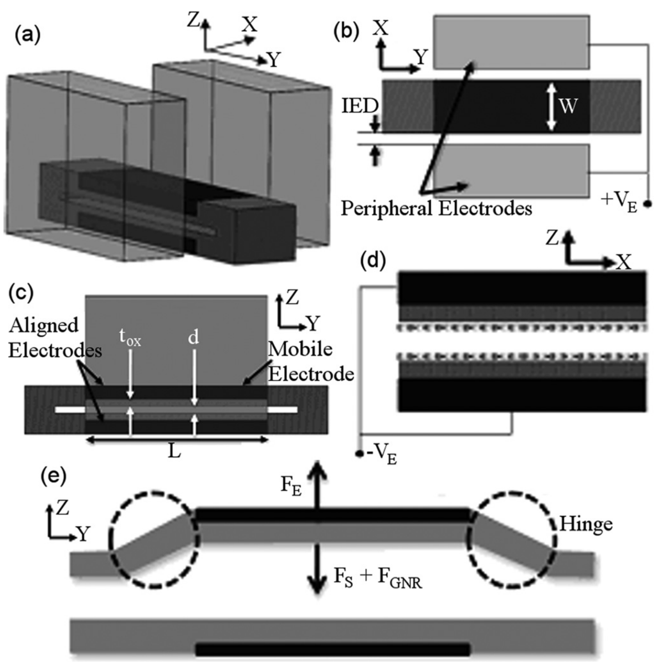


FIG. 6. (a) 3D view of the device structure. The BGNR is placed in the air gap in between the oxide layers. When a voltage of $+V_E$ is applied to the peripheral electrodes and a voltage of $-V_E$ is applied to the aligned electrodes, the top mobile electrode is repelled from the bottom fixed electrode and moves along the $+Z$ direction. (b) Top view of the device showing the peripheral electrodes and the inter-electrode distance (IED). (c) Side view of the device showing the aligned electrodes, the oxide thickness ($t_{ox} = 1$ nm), and the distance of separation $\boldsymbol{d}$ between the two GNR layers. (d) Zoom of the side view showing the BGNR layer. (e) $V_E > V_{TH}$. The switch is in OFF-state, showing the balancing of the forces.

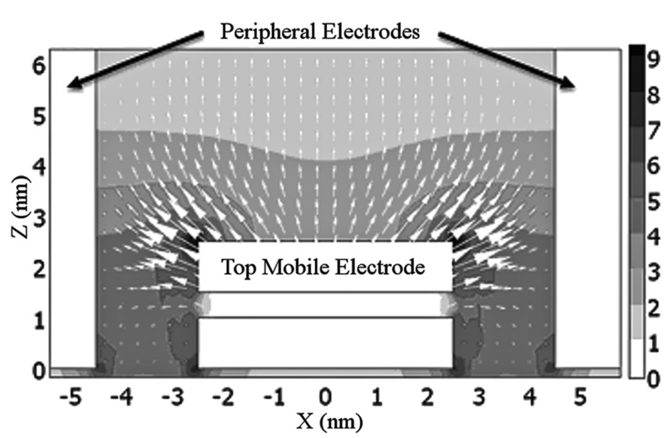


FIG. 7. Plot of the electric field with arrows showing the direction and relative magnitude of displacement of the top movable electrode. The gradation bar represents the electric field in V/nm.

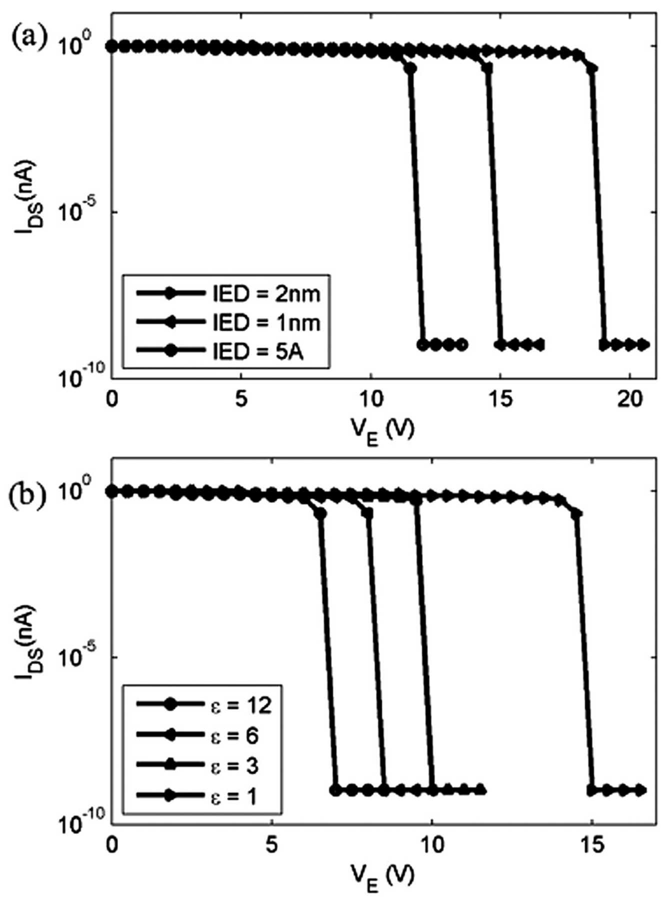


FIG. 8. *I-V* curves showing (a) the effect of varying IED. A reduction in the IED causes an increase in $C$, and hence the $V_{TH}$ is reduced. (b) The effect of increasing the dielectric constant $\varepsilon$ of the ambient using liquid packaging (IED = 1 nm). A larger $\varepsilon$ increases $C$ and thus lowers the $V_{TH}$.

Next, we investigate the possible approaches to adjusting $V_{TH}$ by varying $C$ in (4). To achieve this purpose, one can either bring the peripheral electrodes closer together, resulting in a reduced inter-electrode distance (IED), or increase the dielectric constant of the ambient with the use of a special liquid packaging technique.[26] These two approaches increase $C$ and result in an increase in $F_E$. The effect of reducing the IED is shown in Fig. 8(a), in which an aggressive $V_{TH}$ reduction is observed. When the IED is reduced from 2 nm to 5 Å, $V_{TH}$ decreases from 19 to 12 V. However, an IED = 1 nm is used in subsequent modeling, as it is physically easier to achieve with current technology. The effect of increasing the dielectric constant of the ambient by using a liquid packaging is next explored in Fig. 9(b). The $V_{TH}$ is reduced from 15 V for the air package to 7 V for an ambient dielectric constant of 12. By using liquids with a higher dielectric constant for packaging, the $V_{TH}$ can be potentially reduced even further.

Finally, we would like to note that unlike in the case of CPP actuators, in which the $V_{TH}$ increases with increasing electrode area due to the increased capacitances, simulation studies on the effect of varying the geometries ($W$ and $T$) in the ERF model (IED = 1 nm and ambient dielectric constant of 12) for values of $W$ = 10 and 15 nm and $T$ = 5, 15, and 20 nm revealed that the generated $F_E$ shows very slight variations from the original case ($W$ = 5 nm and $T$ = 10 nm), and the value of $V_{TH}$ does not decrease further when these parameters are changed. This is because the force is mainly acting on the edges of the electrode, as shown in Fig. 7, and therefore any area change has a negligible effect on the force. As a result, the values of the IED and the ambient dielectric constant should be optimized based on the requirement on $V_{TH}$.

## IV. CONCLUSION

BGNR NEMS switches are studied in this work, and their device working principles are briefly introduced. The electronic structure of BGNR can be modified after fabrication by changing the interlayer distance, and this acts as the operating principle for the NEMS switch. In this study, we examined two device designs based on the capacitive parallel plate actuator and the electrostatic repulsive force actuator, and the device performances are examined through analytic equations and finite element method simulation, respectively. Although the CPP design provides a simpler implementation, its performance is limited by the size of the gate area and, therefore, the capacitance, and it suffers from the risk of stiction between the mobile and fixed electrodes. On the other hand, the more complex design of the ERF actuator provides a more stable switching mechanism and eliminates the gate area requirement. Finally, device optimization, in terms of the tuning of $V_{TH}$, is also studied by varying the different parameters in the devices. Such small scale switches with a large ON-OFF ratio and tunable switch biases have great potential in low power memory and sensor applications.

## ACKNOWLEDGMENTS

The computations were performed on the cluster at the Computational Nanoelectronics and Nano-device Laboratory of the National University of Singapore. This work is supported by the Science and Engineering Research Council, Agency for Science, Technology and Research, Singapore under Grant Nos. 0821010023 and 1021010022.

[1]J. D. Meindl, Q. Chen, and J. A. Davis, Science **293**(5537), 2044 (2001).
[2]D. J. Frank, R. H. Dennard, E. Nowak, P. M. Solomon, Y. Taur, and H.-S. P. Wong, Proc. IEEE **89**(3), 259 (2001).
[3]T. Rueckes, K. Kim, E. Joselevich, G. Y. Tseng, C. L. Cheung, and C. Lieber, Science **289**(5476), 94 (2000).
[4]R. L. Badzey, G. Zolfagharkhani, A. Gaidazhy, and P. Mohanty, Appl. Phys. Lett. **85**(16), 3587 (2004).
[5]J. E. Jang, S. N. Cha, Y. Choi, T. P. Butler, D. J. Kang, D. G. Hasko, J. E. Jung, J. M. Kim, and G. A. J. Amaratunga, Tech. Dig. - Int. Electron Devices Meet. 261 (2005).
[6]M. A. Beunder, R. van Kampen, D. Lacey, M. Renault, and C. G. Smith, *Non-Volatile Memory Technology Symposium*, (Dallas, Texas, USA, 10 November 2005), p. 68.
[7]Z. Lee, C. Ophus, L. M. Fischer, N. Nelson-Fitzpatrick, K. L. Westra, S. Evoy, V. Radmilovic, U. Dahmen, and D. Mitlin, Nanotechnology **17**(12), 3063 (2006).
[8]W. W. Jang, J. O. Lee, J.-B. Yoon, M.-S. Kim, J.-M. Lee, S.-M. Kim, K.-H. Cho, D.-W. Kim, D. Park, and W.-S. Lee, Appl. Phys. Lett. **92**(10), 103110 (2008).
[9]A. H. Castro Neto, F. Guinea, N. M. R Peres, K. S. Novoselov, and A. K. Geim, Rev. Mod. Phys. **81**(1), 109 (2009).

[10]K. S. Novoselov, A. K. Geim, S. V. Morozov, D. Jiang, Y. Zhang, S. V. Dubonos, I. V. Grigorieva, and A. A. Firsov, Science **306**(5696), 666 (2004).
[11]C. Berger, Z. Song, X. Li, X. Wu, N. Brown, C. Naud, D. Mayou, T. Li, J. Hass, A. N. Marchenkov, E. H. Conrad, P. N. First, and W. A. de Heer, Science **312**(5777), 1191 (2006).
[12]M. C. Lemme, T. J. Echtermeyer, M. Baus, and H. Kurz, IEEE Electron Device Lett. **28**(4), 282 (2007).
[13]J. S. Bunch, A. M. van der Zande, S. S. Verbridge, I. W. Frank, D. M. Tanenbaum, J. M. Parpia, H. G. Craighead, and P. L. McEuen, Science **315**(5811), 490 (2007).
[14]C. Chen, S. Rosenblatt, K. I. Bolotin, P. Kim, I. Kymissis, H. L. Stormer, T. F. Heinz, and J. Hone, Tech. Dig. - Int. Electron Devices Meet. 253 (2009).
[15]M. Dragoman, D. Dragoman, F. Coccetti, R. Plana, and A. A. Muller, J. Appl. Phys. **105**(5), 054309 (2009).
[16]K.-T. Lam and G. Liang, Appl. Phys. Lett. **92**(22), 223106 (2008).
[17]B. Sahu, H. Min, A. H. MacDonald, and S. K. Banerjee, Phys. Rev. B **78**(4), 045404 (2008).
[18]K.-T. Lam, C. Lee, and G. Liang, Appl. Phys. Lett. **95**(14), 143107 (2008).
[19]K. B. Lee and Y.-H. Cho, J. Microelectromech. Syst. **10**(1), 128 (2001).
[20]Q. Yan, B. Huang, J. Yu, F. Zheng, J. Zang, J. Wu, B.-L. Gu, F. Liu, and W. Duan, Nano Lett. **7**(6), 1469 (2007).
[21]J. M. Soler, E. Artacho, J. D. Gale, A. García, J. Junquera, P. Ordejón, and S. Sánchez-Portal, J. Phys. Condens. Matter **14**(11), 2745 (2002).
[22]J. Taylor, H. Guo, and J. Wang, Phys. Rev. B **63**(24), 245407 (2001).
[23]COMSOL AB, MEMS Module, COMSOL, Inc., Burlington, MA, 2007.
[24]M.-H. Bao, *Micro Mechanical Transducers* (Elsevier, Amsterdam, 2000), Chapter IV, pp. 139–198.
[25]S. He and R. B. Mrad, J. Microelectromech. Syst. **17**(3), 532 (2008).
[26]J.-O. Lee, M.-W. Kim, S.-D. Ko, H.-O. Kang, W.-H. Bae, M.-H. Kang, K.-N. Kim, D.-E. Yoo, and J.-B. Yoon, Tech. Dig. - Int. Electron Devices Meet. 227 (2009).